https://doi.org/10.5194/egusphere-2025-5837
Preprint. Discussion started: 14 January 2026
© Author(s) 2026. CC BY 4.0 License.

Spatiotemporal optimization of NO_x and VOC emissions using a hybrid inversion framework and its implication for ozone sensitivity diagnosis

Jeonghyeok Moon[1], Wonbae Jeon[2,3], Sujong Jeong[4,5,6], Yunsoo Choi[7], Hyun Cheol Kim[8,9], Soon-Young Park[10], Juseon Bak[11], Jung-Woo Yoo[11], Jaehyeong Park[12], Dongjin Kim[2,12], Hyeonsik Choe[2,12], Chae-Yeong Yang[2,12], Min Heo[2,12]

[1]Environmental Planning Institute, Seoul National University, Seoul 08826, South Korea
[2]BK21 School of Earth and Environmental System, Pusan National University, Busan 46241, South Korea
[3]Department of Atmospheric Sciences, Pusan National University, Busan 46241, South Korea
[4]Department of Environmental Management, Graduate School of Environmental Studies, Seoul National University, Seoul, 08826, South Korea
[5]Climate Tech Center, Seoul National University, Seoul, 08826, South Korea
[6]Institute for Sustainable Development, Seoul National University, Seoul, 08826, South Korea
[7]Department of Earth and Atmospheric Sciences, University of Houston, Houston, TX 77204, USA
[8]Air Resources Laboratory, National Oceanic and Atmospheric Administration, College Park, MD, 20740, USA
[9]Cooperative Institute for Satellite Earth System Studies, University of Maryland, College Park, MD, 20742, USA
[10]Department of Science Education, Daegu National University of Education, Daegu, 42411, South Korea
[11]Institute of Environmental Studies, Pusan National University, Busan 46241, South Korea
[12]Division of Earth Environmental System, Pusan National University, Busan 46241, South Korea

Correspondence to: Wonbae Jeon (wbjeon@pusan.ac.kr)

Abstract. Ozone (O_3) over South Korea has risen in recent years, underscoring the need to accurately quantify emissions of nitrogen oxides (NO_x) and volatile organic compounds (VOC). We develop a hybrid inverse modeling framework that couples the Finite Difference Mass Balance (FDMB) method with four-dimensional variational (4D-Var) assimilation using the Community Multiscale Air Quality (CMAQ) model to jointly constrain spatiotemporal NO_x and VOC emissions. The inversion is constrained by Tropospheric Monitoring Instrument (TROPOMI) NO_2 and HCHO columns and by surface NO_2 and O_3 from the Air Quality Monitoring Station (AQMS) network. The analysis covers 1–14 May 2022, a period of climatologically high O_3. Optimized NO_x emissions exhibit strong diurnal adjustments relative to the prior (nighttime reductions up to 51 % and daytime increases up to 14 %). The joint inversion of NO_x and VOC delivers the largest improvement in O_3 simulations, achieving the best agreement with observations (IOA > 0.8). Constrained emissions shift O_3 sensitivity from VOC-sensitive to NO_x-sensitive across much of the domain, improving spatial consistency with TROPOMI-derived formaldehyde-to-NO_2 ratio (FNR) diagnostics. Adjoint-based hourly ΔO_3 responses reveal regime- and hour-dependent behavior: VOC controls are most effective under VOC-sensitive conditions, whereas NO_x controls are more direct under NO_x-sensitive conditions. Importantly, because O_3 titration is immediate while photochemical production requires finite reaction time, emissions released approximately 1–2 hours earlier have the greatest influence on current O_3, motivating hour-specific, regime-specific controls.

https://doi.org/10.5194/egusphere-2025-5837
Preprint. Discussion started: 14 January 2026
© Author(s) 2026. CC BY 4.0 License.

Overall, the hybrid framework improves O_3 simulations and sensitivity-regime diagnosis, enabling spatiotemporally resolved precursor emission reduction guidance for effective O_3 mitigation.

1 Introduction

Surface ozone (O_3) is a highly reactive secondary air pollutant primarily formed through complex photochemical reactions involving nitrogen oxides ($NO_x \equiv NO + NO_2$) and volatile organic compounds (VOC). Elevated O_3 concentrations have been associated with adverse respiratory health outcomes, including asthma and pneumonia, as well as broader impacts on air quality and ecosystem health (Gryparis et al., 2004; Turner et al., 2016; Raza et al., 2018). In recent years, a persistent increase in O_3 levels has been observed across East Asia, leading to a growing demand for scientific investigation into its underlying causes. Previous studies have attributed this increase to multiple factors, including changes in atmospheric circulation patterns due to climate change, enhanced stratosphere–troposphere exchange, and shifts in the O_3 sensitivity regime (Lee et al., 2021; Itahashi et al., 2022; Hou et al., 2023).

Among these factors, shifts in the O_3 sensitivity regime play a key role in understanding the causes of rising recent O_3 levels. The O_3 sensitivity regime refers to the relative responsiveness of O_3 formation to changes in its precursor emissions, primarily NO_x and VOC. In a VOC-sensitive regime, O_3 production increases when VOC emissions rise, but shows little change or even decreases when NO_x emissions are reduced. Conversely, in a NO_x-sensitive regime, O_3 formation responds strongly to reductions in NO_x emissions. Several recent studies have reported that many regions in East Asia are currently undergoing a transition from a VOC-sensitive regime toward a NO_x-sensitive or transitional regime, wherein reductions in NO_x emissions paradoxically result in increased O_3 concentrations (Lee et al., 2021; Itahashi et al., 2022; Wang et al., 2025). Accordingly, the formulation of effective O_3 mitigation strategies necessitates accurate characterization of region-specific sensitivity regimes, which in turn requires an accurate spatiotemporal estimation of NO_x and VOC emissions.

Emission estimates are typically derived using either bottom-up or top-down approaches. The bottom-up method relies on activity data and emission factors to statistically estimate emissions. While widely used, this approach is subject to high uncertainty due to variability in emission factors, spatial heterogeneity in activity data, and the extensive time and cost required to survey all emission sources (Zhao et al., 2011; Hristov et al., 2017; Solazzo et al., 2021). To overcome these limitations, top-down approaches based on inverse modeling have become increasingly prevalent. These methods assimilate satellite and ground-based observational data with chemical transport models to infer emissions that are consistent with observed atmospheric concentrations (Miller et al., 2014; Cheng et al., 2021). Various inverse modeling techniques have been proposed, including mass balance (Cooper et al., 2017; Li et al., 2019; Qu et al., 2019; Momeni et al., 2024), four-dimensional variational assimilation (4D-Var) (Hu et al., 2022; Voshtani et al., 2023; Nüß et al., 2025), and ensemble Kalman filter (EnKF) methods (Peng et al., 2017; Jia et al., 2022; Wu et al., 2023). The mass balance approaches are computationally efficient and suitable for rapid emission updates, but are known to be susceptible to smearing effects due to pollutant transport (Cooper et al., 2017). Among the mass balance-based methods, the Finite Difference Mass Balance (FDMB) method has been shown to improve

https://doi.org/10.5194/egusphere-2025-5837
Preprint. Discussion started: 14 January 2026
© Author(s) 2026. CC BY 4.0 License.

emission estimates by exploiting sensitivities between emissions and column concentrations (Cooper et al., 2017; Mun et al., 2023). In contrast, the 4D-Var approach uses adjoint sensitivity to trace the influence of emission sources backward in time, thereby reducing transport-induced smearing errors (Li et al., 2019). However, it is computationally intensive and requires the development of an adjoint model, which can be a substantial limitation. To leverage the strengths of both approaches, a hybrid inverse modeling framework combining the mass balance and the 4D-Var have been recently proposed (Chen et al., 2021; Choi et al., 2022; Moon et al., 2024).

Nevertheless, most inverse modeling studies have focused primarily on correcting the spatial distribution of emissions, with limited consideration of their temporal variability. This remains a critical limitation, particularly for O_3, which is both short-lived and chemically reactive. Diurnal variations in precursor emissions can strongly influence O_3 formation due to nonlinear photochemical processes (Wang et al., 2018). Moreover, because O_3 production is jointly controlled by NO_x and VOC, accurately reproducing O_3 concentrations requires not only capturing the temporal evolution of emissions but also constraining the contributions of both precursor species. Therefore, accurate analysis of O_3 distributions requires a comprehensive inverse modeling framework capable of simultaneously optimizing the spatiotemporal distribution of both NO_x and VOC emissions.

In this study, we develop a hybrid inverse modeling framework that combines the FDMB and 4D-Var methods with the Community Multiscale Air Quality (CMAQ) model to simultaneously constrain the spatiotemporal distributions of NO_x and VOC emissions over South Korea, to improve O_3 simulations and sensitivity regime diagnostics, and to quantify hourly ΔO_3 responses to NO_x and VOC emissions using adjoint sensitivities. Here, ΔO_3 represents the change in O_3 concentration attributable to a unit perturbation in precursor emissions, as diagnosed by the adjoint model. The inverse modeling system is constrained using satellite-based measurements from the TROPOspheric Monitoring Instrument (TROPOMI) and in situ observations from the Air Quality Monitoring Station (AQMS) network. We further analyze the changes in O_3 concentrations and O_3 sensitivity regimes before and after inverse modeling to propose a robust top-down emission adjustment approach that can inform the development of future O_3 mitigation policies. The results are presented in four sections: (1) spatiotemporal changes in emissions (Section 3.1), (2) spatiotemporal changes in NO_2, HCHO, and O_3 concentrations (Section 3.2), (3) improvement of O_3 sensitivity regimes through hybrid inversion (Section 3.3), and (4) regime-dependent hourly ΔO_3 responses to NO_x and VOC emissions (Section 3.4).

2 Methods

2.1 WRF/CMAQ modeling system

In this study, we employed version 5.0 of the Community Multiscale Air Quality (CMAQ) model, developed by the U.S. Environmental Protection Agency (EPA), which includes an adjoint model, to conduct 4D-Var inverse modeling (Zhao et al., 2020). Meteorological input fields required for the CMAQ simulation were generated using the Weather Research and Forecasting (WRF) model version 3.8.1 (Skamarock et al., 2008). The modeling domains consisted of two nested grids: a

https://doi.org/10.5194/egusphere-2025-5837
Preprint. Discussion started: 14 January 2026
© Author(s) 2026. CC BY 4.0 License.

coarse-resolution outer domain (D1) covering East Asia and a finer-resolution inner domain (D2) focusing on South Korea (Fig. 1).

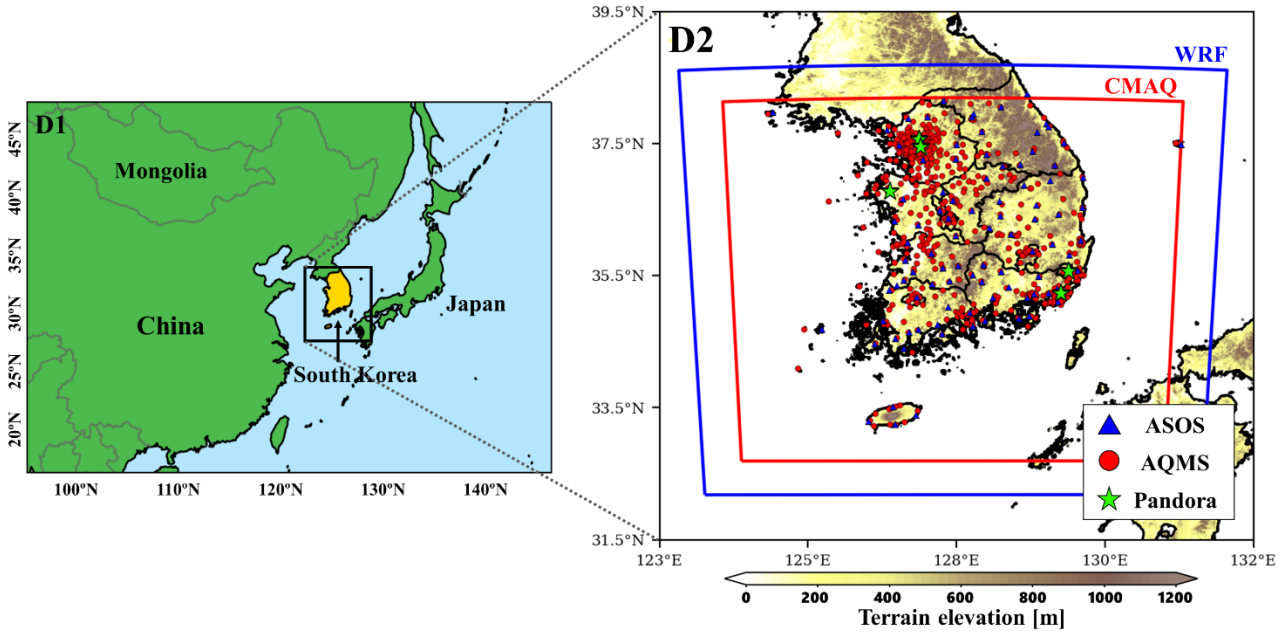

Figure 1: WRF/CMAQ modeling domains and spatial distribution of observational sites (ASOS: blue triangles; AQMS: red circles; Pandora: green stars).

This study targeted South Korea, and the inverse modeling was conducted exclusively over D2. The initial and boundary conditions for the WRF simulation were obtained from the ERA5 reanalysis dataset with a spatial resolution of 0.25° × 0.25°, provided by the European Centre for Medium-Range Weather Forecasts (ECMWF) (Hersbach et al., 2023a, b). To improve the accuracy of meteorological fields, grid nudging was applied during WRF simulations (Jeon et al., 2015).

We utilized the Emissions Database for Global Atmospheric Research-Hemispheric Transport of Air Pollution version 3 (EDGAR-HTAPv3) as the source of anthropogenic emissions. This inventory incorporates national emission estimates from South Korea's Clean Air Policy Support System (CAPSS) and provides monthly averaged emissions at a spatial resolution of 0.1° × 0.1° for nine key air pollutants: BC, CO, NO_x, SO_2, NH_3, OC, NMVOC (non-methane volatile organic compounds) or, PM_{10}, and $PM_{2.5}$ (Crippa et al., 2023). To generate the hourly gridded emissions required for CMAQ modeling, the monthly data were temporally downscaled using sector-specific temporal allocation profiles (Crippa et al., 2020). In addition, biogenic volatile organic compound (BVOC) emissions, which serve as key precursors of O_3, were estimated using the Model of Emissions of Gases and Aerosols from Nature (MEGAN) version 2.1 (Guenther et al., 2012).

https://doi.org/10.5194/egusphere-2025-5837
Preprint. Discussion started: 14 January 2026
© Author(s) 2026. CC BY 4.0 License.

The modeling period was set to May 1–14, 2022 (two weeks), selected for computational efficiency during the month that recorded the highest monthly average surface O_3 concentrations over South Korea in the past decade (Fig. S1). Detailed model configurations for both WRF and CMAQ are provided in Tables S1 and S2.

2.2 Observation data

2.2.1 Ground-based observations

For the evaluation of meteorological and air quality model performance and the implementation of inverse modeling over South Korea, we utilized ground-based observational data from Automated Surface Observing System (ASOS), Air Quality Monitoring Stations (AQMS), and Pandora spectrometers (Fig. 1). Hourly measurements of temperature, wind speed, and relative humidity from 95 ASOS sites were used to assess the accuracy of meteorological simulations. For air quality model evaluation and inverse modeling, we obtained hourly NO_2 and O_3 concentrations from 619 AQMS sites.

In addition, tropospheric HCHO Vertical Column Densities (VCDs) were obtained from Pandora spectrometers at five sites operated by the Pandonia Global Network (PGN) to evaluate the model's performance in simulating VOC. To ensure data reliability, only Pandora HCHO retrievals with Level 2 (L2) data quality flags classified as "high" (0, 10) or "medium" (1, 11) were used in this study (Bae et al., 2025; Fu et al., 2025). The Pandora observations were hourly averaged for comparison with model results.

2.2.2 TROPOMI NO_2 and HCHO observations

TROPOMI is the single payload aboard the European Space Agency (ESA)'s Sentinel-5 Precursor (S5P) satellite, launched on October 13, 2017 (Veefkind et al. 2012). Operating in a sun-synchronous polar orbit at an altitude of approximately 800 km, it provides daily global coverage with a high spatial resolution footprint of 5.5 km × 3.5 km at nadir and an equator crossing time near 13:30 local solar time.

Tropospheric VCDs of NO_2 and HCHO used in this study are obtained from the TROPOMI Level 2 operational products (De Smedt et al., 2021; van Geffen et al., 2022). Both products are retrieved using a three-step Differential Optical Absorption Spectroscopy (DOAS) technique: (1) fitting of the Slant Column Density (SCD), (2) separation of the tropospheric components from the total SCD, and (3) conversion from slant to vertical column using an air mass factor (AMF). The retrieval accuracy of VCD is highly sensitive to the a priori vertical profile used in the AMF calculation. In the operational products, these profiles are derived from global simulations of the TM5-MP chemistry model at a coarse resolution of 1° × 1°, which is much coarser than the native resolution of the TROPOMI SCDs. This spatial mismatch has been linked to underestimation of VCDs, particularly over regions with strong or localized emissions (Judd et al., 2020; Douros et al., 2023; Goldberg et al., 2024).

To mitigate this limitation, we recalculate the satellite VCDs using Eq. (1) (Souri et al., 2016), which adjusts the satellite-derived VCDs ($VCD_{satellite}$) by accounting for differences between the a priori profiles used in the satellite retrieval and those from a regional chemical transport model.

https://doi.org/10.5194/egusphere-2025-5837
Preprint. Discussion started: 14 January 2026
© Author(s) 2026. CC BY 4.0 License.

$$VCD'_{satellite} = \frac{VCD_{satellite} \times AMF_{satellite}}{AMF_{model}} \quad (1)$$

$AMF_{satellite}$ is the AMF provided in the TROPOMI Level 2 product, and AMF_{model} is a model-derived AMF calculated using the vertical profile from the CMAQ model and the TROPOMI Averaging Kernel (AK) (Eq. (2)).

$$AMF_{model} = AMF_{apriori} \frac{\sum AK \times VCD_{model}}{\sum VCD_{model}} \quad (2)$$

To ensure data quality, we applied a quality assurance threshold of qa_value > 0.75 for NO_2 (high quality), which is relaxed to > 0.5 for HCHO (moderate quality) to retain sufficient sampling.

2.3 Inverse modeling

2.3.1 Finite Difference Mass Balance inversion using 3D-Var

The mass balance approach estimates emissions by assuming a linear relationship between observed column concentrations and surface emissions (Cooper et al., 2017). Among the mass balance-based methods, the Finite Difference Mass Balance (FDMB) method, proposed by Lamsal et al., (2011), introduces a scaling factor (β) to account for nonlinear relationships between changes in column concentrations (ΔΩ) and emissions (ΔE) (Eqs. (3) and (4)).

$$E_{FDMB} = E_m \left(1 + \frac{\Omega_o - \Omega_m}{\beta \Omega_m}\right) \quad (3)$$

$$\beta = \frac{\Delta\Omega_m / \Omega_m}{\Delta E_m / E_m} \quad (4)$$

Here, E_{FDMB} represents the FDMB emissions, E_m is the a priori model emissions, Ω_o is the observed column density, and Ω_m is the simulated column density. The sensitivity factor β is calculated from simulations using the prior emissions (E_m) and emissions perturbed by 10 %. β value is constrained between 0.1 and 10 to prevent unrealistic corrections (Cooper et al., 2017; Li et al., 2019; Mun et al., 2023).

In this study, we applied the FDMB inversion to jointly constrain NO_x and VOC emissions. We first optimized NO_x emissions by deriving an emission factor based on the sensitivity of NO_2 columns to NO_x emissions (Eq. (5)). For VOC, total emissions were separated into anthropogenic VOC (AVOC) and BVOC, as the two categories have distinct VOC species compositions that lead to different HCHO responses (Millet et al., 2006; Choi et al., 2022; Oomen et al., 2024). We then independently quantified the HCHO column sensitivities to AVOC and BVOC emissions (Eqs. (6) and (7)). Based on these sensitivities, we derived emission factors for both AVOC and BVOC components.

$$\beta_{NO_x} = \frac{\Delta\Omega_{NO_2} / \Omega_{NO_2}}{\Delta E_{NO_x} / E_{NO_x}} \quad (5)$$

$$\beta_{AVOC} = \frac{\Delta\Omega_{HCHO} / \Omega_{HCHO}}{\Delta E_{AVOC} / E_{AVOC}} \quad (6)$$

$$\beta_{BVOC} = \frac{\Delta\Omega_{HCHO} / \Omega_{HCHO}}{\Delta E_{BVOC} / E_{BVOC}} \quad (7)$$

However, traditional mass balance approaches may incorporate biases inherent in satellite observations into the inferred emission estimates. To address this limitation, East et al. (2022) applied the FDMB inversion using an analysis field generated

https://doi.org/10.5194/egusphere-2025-5837
Preprint. Discussion started: 14 January 2026
© Author(s) 2026. CC BY 4.0 License.

via three-dimensional variational (3D-Var) assimilation as the observational constraint. In this study, we generated a 3D-Var-based analysis field to minimize observational uncertainties and employed it as the constraint in the FDMB inversion process (Fig. 2).

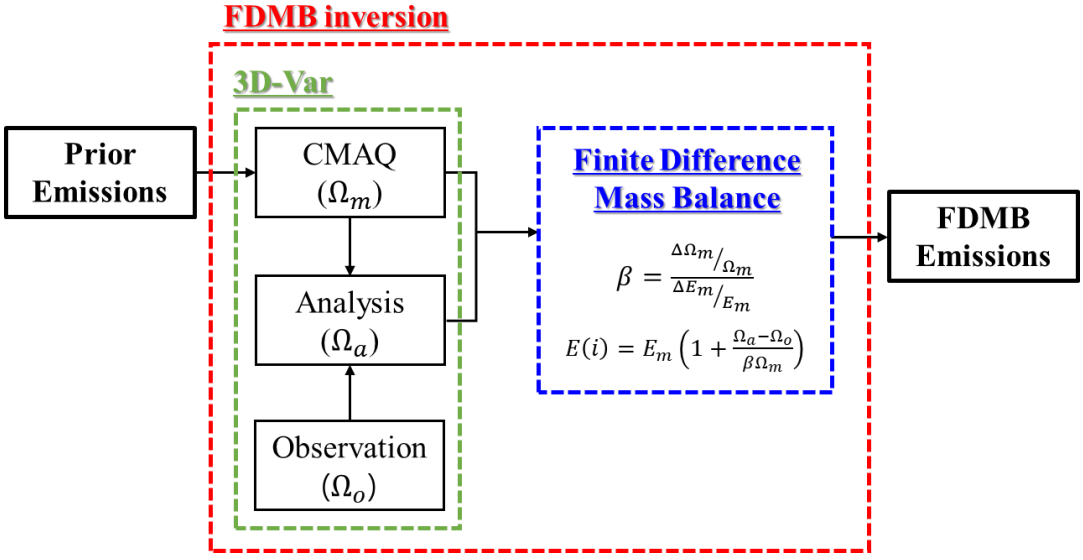

Figure 2: Flowchart of the FDMB inversion framework with 3D-Var assimilation. Red boxes denote the FDMB inversion process, green boxes represent the 3D-Var assimilation (Ω_m: CMAQ VCD, Ω_o: observed VCD, Ω_a: analysis VCD), and blue boxes indicate the FDMB process that updates emissions using finite-difference sensitivities.

Furthermore, to minimize errors associated with the smearing effect caused by atmospheric transport, the FDMB inversion was performed using a two-week-averaged column density over the study period. Consequently, this study focused on constraining the spatial distribution of emissions based on temporally averaged observations, without accounting for temporal variability in emissions.

2.3.2 4D-Var inversion

While the FDMB inverse modeling enables spatial correction of emissions effectively, it cannot account for their temporal variability. To overcome this limitation, we implemented a four-dimensional variational (4D-Var) inversion approach to constrain the spatial and temporal distribution of emissions. The cost function employed in this study is defined in Eq. (8).

$$J(\alpha) = \frac{1}{2}\gamma\sum_{i=0}^{n}(\alpha_i - 1)^T B_{e_i}^{-1}(\alpha_i - 1) + \frac{1}{2}\sum_{t=1}^{n+1}\sum_{i=t}^{n+1}(y_i^o - H_{i-1}(e_{i-1}))^T R_i^{-1}(y_i^o - H_{i-1}(e_{i-1})) \quad (8)$$

Here, the control variable is the emission (e) over a defined time window (n), and the emission scaling factor ($\alpha = e/e^b$) represents the ratio between the updated and prior emissions. H denotes the observation operator, y is the observation vector, and B and R are the error covariance matrices for emissions and observations, respectively. Assuming spatial independence,

https://doi.org/10.5194/egusphere-2025-5837
Preprint. Discussion started: 14 January 2026
© Author(s) 2026. CC BY 4.0 License.

both B and R were configured as diagonal matrices. The emission uncertainties were set to 100 % of the prior emissions. For ground-based AQMS observations, the total observational error was estimated as the sum of measurement errors with representativeness errors (Elbern et al., 2007; Feng et al., 2018).

In this study, the assimilation time window was set to 24 hours to better represent diurnal variations in atmospheric processes. To prevent overfitting or underfitting in the inversion process, a regularization parameter γ was introduced (Henze et al., 2009; Chen et al., 2021; Yu et al., 2021), and its optimal value was determined using the L-curve test (Hansen, 1999). The optimized γ was then used to constrain the spatiotemporal distribution of emissions, ensuring physically realistic corrections.

2.3.3 Hybrid inverse modeling framework

In this study, we applied the hybrid inverse modeling framework proposed by Moon et al. (2024) to constrain the spatiotemporal distribution of NO_x and VOC, which are key precursors influencing O_3 formation and destruction. The hybrid inverse modeling approach consists of a two-step process: an initial adjustment of the spatial distribution of emissions using the FDMB method, followed by a refinement of the spatiotemporal distribution through 4D-Var inverse modeling. While previous studies have primarily focused on single-species corrections such as CO or NO_2, we extended the approach to jointly optimize both NO_x and VOC emissions to better represent the nonlinear photochemical processes governing O_3 formation. A schematic of the hybrid inverse modeling framework is shown in Fig. 3.

First, we performed FDMB inversions for NO_x and VOC emissions in two sequential steps. In the first step, TROPOMI NO_2 VCDs were used to update the spatial distribution of NO_x emissions. In the second step, TROPOMI HCHO VCDs were utilized to correct VOC emissions. Given the different source characteristics of VOC, we estimated separate scaling factors for AVOC and BVOC.

Next, the FDMB NO_x and VOC emissions were used as the prior estimate for a 4D-Var inversion. In this step, we assimilated hourly NO_2 and O_3 measurements from the AQMS network, which are highly sensitive to changes in NO_x and VOC emissions. The control variables in the 4D-Var system included both NO_x and 15 VOC species (Table S3), enabling the joint optimization of key precursors that drive O_3 formation and variability.

To evaluate the effectiveness of the hybrid inverse modeling approach, we designed three experiments: (1) Prior, which used the prior emissions; (2) Hybrid_NOx, which corrected only NO_x emissions; and (3) Hybrid_NOx+VOC, which jointly constrained NO_x and VOC emissions. By comparing the model outputs from both experiments with observations, we quantified the relative contributions of each precursor to changes in the spatiotemporal distribution of O_3 and its sensitivity regime. Model performance was assessed using multiple statistical metrics (Table S4).

https://doi.org/10.5194/egusphere-2025-5837
Preprint. Discussion started: 14 January 2026
© Author(s) 2026. CC BY 4.0 License.

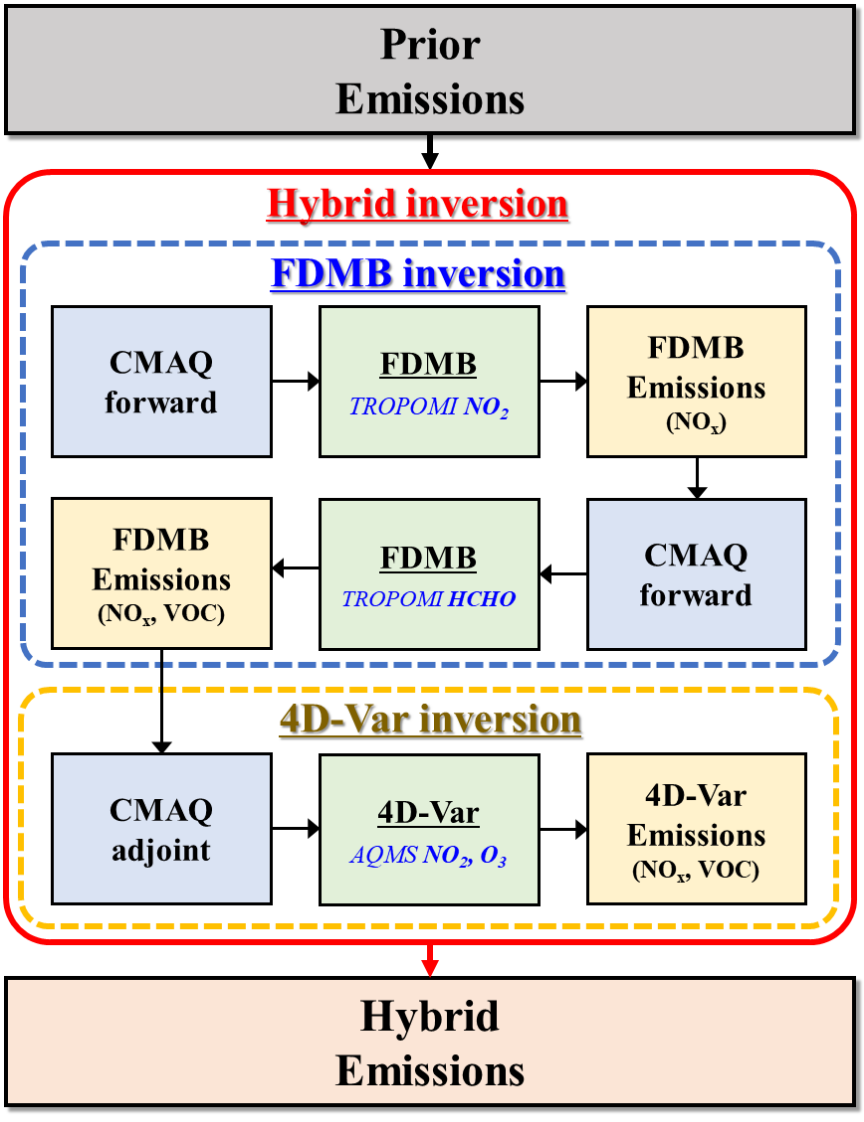

Figure 3: Schematic of the hybrid inverse modeling framework combining FDMB and 4D-Var inversions. In the first step, the FDMB inversion (blue box) corrects the spatial distribution of NO_x and VOC emissions using TROPOMI NO_2 and HCHO VCDs. In the second step, the 4D-Var inversion (Yellow box) constrains the spatiotemporal distribution of NO_x and VOC emissions by assimilating hourly ground-based NO_2 and O_3 observations.

2.4. O_3 sensitivity regime classification

The O_3 sensitivity regime can be classified based on the VOC/NO_x ratio, for which several photochemical indicators—such as HCHO/NO_2, H_2O_2/HNO_3, and H_2O_2/NO_y—have been widely applied (Sillman, 1995; Liu and Shi, 2021). Among these, the HCHO-to-NO_2 ratio (FNR) has been widely used because it is applicable to satellite observations and can effectively capture

https://doi.org/10.5194/egusphere-2025-5837
Preprint. Discussion started: 14 January 2026
© Author(s) 2026. CC BY 4.0 License.

regional-scale photochemical conditions (Duncan et al., 2010; Liu et al., 2021; Jang et al., 2023; Rahman et al., 2025). In this study, we assess the model's capability to diagnose O_3 sensitivity regimes by comparing FNR values derived from TROPOMI satellite measurements with those simulated by the model. Conventionally, we classified FNR values ≤ 2.0 as VOC-sensitive, ≥ 2.8 as NO_x-sensitive, and between 2.0 and 2.8 as neutral, following the thresholds proposed by Jang et al. (2023) for South Korea.

2.5. Adjoint-based analysis of ΔO_3 responses to precursor emissions

We quantified the hourly influence of NO_x and VOC emissions on O_3 as a function of the sensitivity regime using the CMAQ adjoint model driven by posterior emissions (Fig. 4). For each local hour h, the regime-specific cost function $J_r(h)$ was defined as the two-week mean of the spatially averaged surface O_3 over grids classified as regime r at that hour.

$$J_r(h) = \frac{1}{|D|}\sum_{d\in D}\frac{1}{|G_r|}\sum_{g\in G_r} C_{O_3}(g,h,d),\ h \in \{0,1,\dots,23\},\ r \in \{VOC-sensitive, NO_x-sensitive\} \quad (9)$$

Here, D is the set of analysis days (two weeks), G_r is the set of grids classified as regime r, and $C_{O_3}(g,h,d)$ is the surface O_3 concentration at grid g.

A single adjoint integration provides, for a receptor hour t_2, the sensitivities of $J_r(t_2)$ to emissions at all emission hours t_1:

$$S_i(t_1 \to t_2) = \frac{\partial J_r(t_2)}{\partial E_i(t_1)} \quad (10)$$

where $i \in \{NO_x, VOC\}$ and $E_i(t_1)$ is the hourly emission rate. Multiplying these sensitivities by the corresponding emissions yields the emission-time–specific O_3 response:

$$\Delta O_3^{r,i}(t_1,t_2) = S_i(t_1 \to t_2) \times E_i(t_1)\ [ppb] \quad (11)$$

and summing over all emission hours yields the emission-time–integrated response at t_2:

$$\Delta O_{3,all}^{r,i}(t_2) = \sum_{t_1=0}^{23} S_i(t_1 \to t_2) \times E_i(t_1)\ [ppb] \quad (12)$$

In our configuration, S_i has units of ppb per (moles s^{-1}). Responses are evaluated over the grids classified as regime r at the receptor hour t_2, enabling regime-by-regime comparison of NO_x and VOC influences. The adjoint simulations covered the full two-week analysis period. Because each receptor hour requires a distinct adjoint run, we performed 24 adjoint simulations per regime (VOC-sensitive and NO_x-sensitive), for a total of 48 runs. Using the posterior emissions, we then computed and compared regime-, precursor-, and hour-resolved O_3 responses.

https://doi.org/10.5194/egusphere-2025-5837
Preprint. Discussion started: 14 January 2026
© Author(s) 2026. CC BY 4.0 License.

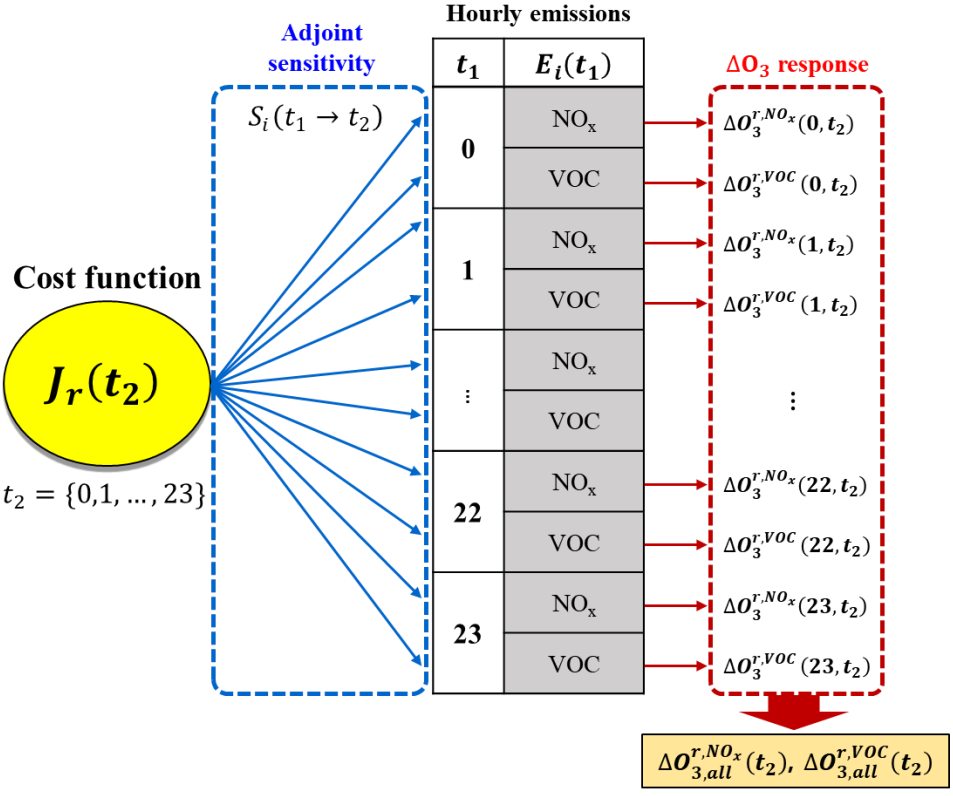

Figure 4: Schematic of the adjoint-based O_3 response calculation. A single adjoint run provides, for a receptor hour t_2, the sensitivities of the regime-mean surface O_3 cost function $J_r(t_2)$ to precursor emissions at each emission hour t_1. Multiplying these sensitivities by the corresponding hourly emissions $E_i(t_1)$ ($i \in \{NO_x, VOC\}$) yields the emission-time–specific O_3 response $\Delta O_3^{r,i}(t_1,t_2)$. Summing over all emission hours $t_1 = 0–23$ gives the emission-time–integrated response $\Delta O_{3,all}^{r,i}(t_2)$. Responses are evaluated over grids classified as regime r at hour t_2, enabling regime-by-regime comparison of NO_x and VOC influences.

3 Results

3.1 Spatiotemporal changes in NO_x and VOC emissions

To investigate the spatiotemporal changes in emissions constrained by the hybrid inverse modeling, we compared the results from the Hybrid_NOx experiment, which constrained only NO_x emissions, and the Hybrid_NOx+VOC experiment, which simultaneously constrained both NO_x and VOC emissions, with those based on the Prior emissions. Prior to the hybrid inversion, an L-curve test was conducted to determine an appropriate γ for the 4D-Var inverse modeling and a value of γ = 10 was selected (Fig. S2).

Figure 5 shows the spatial distributions of NO_x, AVOC, and BVOC emissions averaged over the study period. In the Hybrid_NOx experiment, NO_x emissions were substantially reduced relative to the Prior experiment, particularly over major

https://doi.org/10.5194/egusphere-2025-5837
Preprint. Discussion started: 14 January 2026
© Author(s) 2026. CC BY 4.0 License.

urban regions such as the Seoul Metropolitan Area (SMA), Busan, Ulsan, and Daegu. On average, NO_x emissions across the entire modeling domain decreased by 18.23 %. The Hybrid_NOx+VOC experiment also showed a reduction in NO_x emissions, but to a lesser extent, with an average decrease of 15.50 %. In contrast, VOC emissions remained unchanged in the Hybrid_NOx experiment. However, in the Hybrid_NOx+VOC experiment, emissions of both AVOC and BVOC were substantially increased by approximately 70.54 % and 161.64 %, respectively, relative to the Prior. The increase in AVOC was largely concentrated over urban regions, similar to the NO_x distribution, while BVOC showed a more spatially homogeneous enhancement, especially over vegetated and mountainous areas across South Korea.

The different adjustment magnitudes for AVOC and BVOC emissions in the Hybrid_NOx+VOC experiment arise from the distinct VOC species compositions of the two source categories and the associated differences in their chemical reactivity. Because the HCHO-based optimization updates emissions according to precursor-specific sensitivities, AVOC and BVOC emissions can be adjusted by different amounts. A similar tendency was reported in Choi et al. (2022), where BVOC emissions showed larger adjustments than AVOC when constrained with HCHO column observations. These results indicate that the VOC adjustments in our inversion reflect the species-dependent sensitivities inherent in HCHO-based optimization.

https://doi.org/10.5194/egusphere-2025-5837
Preprint. Discussion started: 14 January 2026
© Author(s) 2026. CC BY 4.0 License.

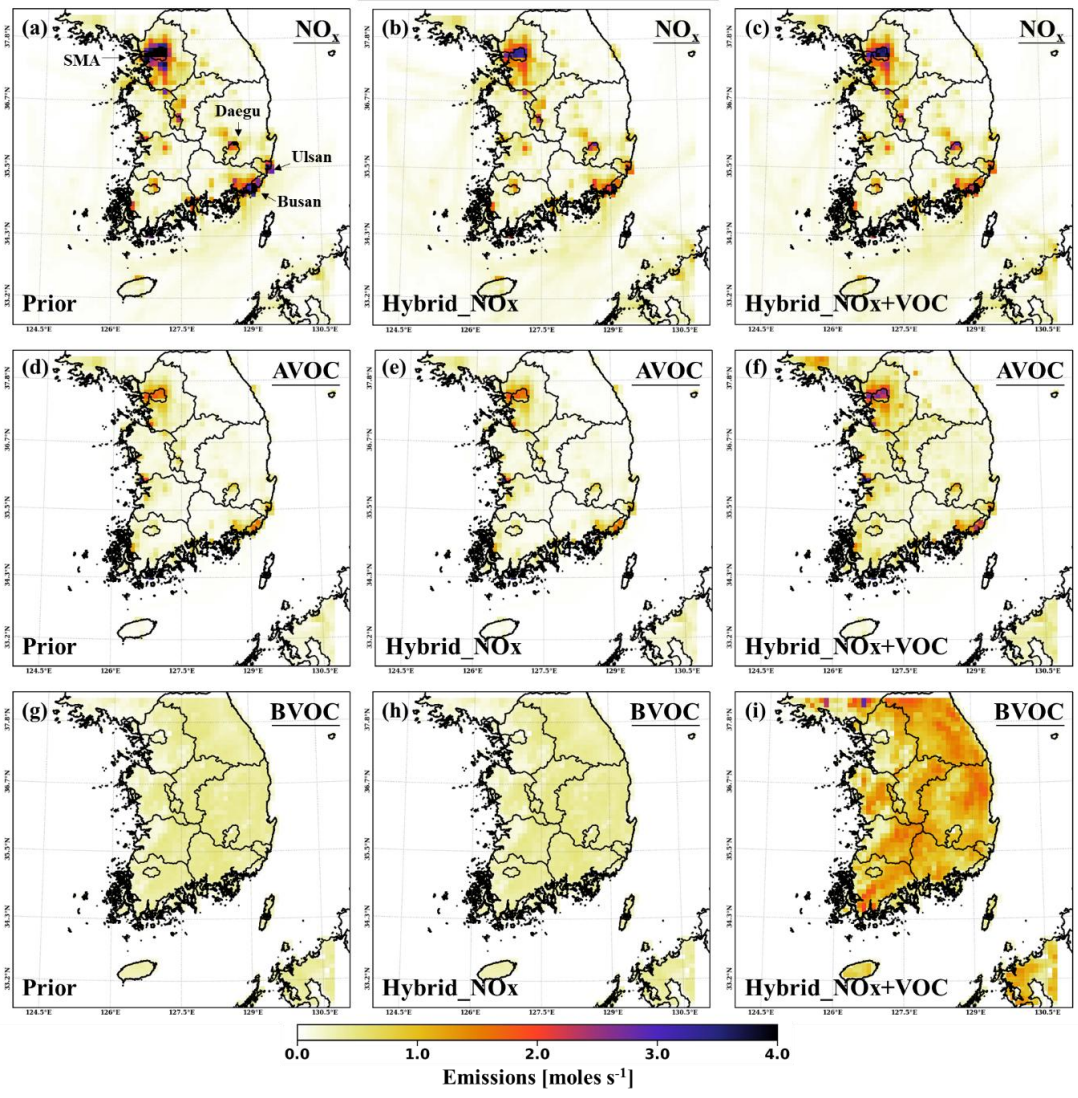

Figure 5: Spatial distributions of (a–c) NO_x, (d–f) AVOC, and (g–i) BVOC emissions, averaged over the study period, for each experiment (Prior, Hybrid_NOx, and Hybrid_NOx+VOC).

295

Figure 6 presents the diurnal variations in NO_x, AVOC, and BVOC emissions for each experiment. The Prior NO_x emissions show two peaks corresponding to morning and evening rush hours. In contrast, the Hybrid_NOx and Hybrid_NOx+VOC experiments exhibit a shift in temporal emission patterns, with increased emissions in the morning and substantial reductions in the evening and at night. This shift implies a redistribution of hourly emission characteristics driven by the inversion process.

300 For VOC, the Hybrid_NOx+VOC experiment resulted in a substantial increase in AVOC emissions during the daytime and a slight increase at night. BVOC emissions, which are primarily driven by photosynthetic and metabolic processes in vegetation, also showed a distinct increase during the daytime, reflecting a temporal pattern similar to that of the Prior emissions.

https://doi.org/10.5194/egusphere-2025-5837
Preprint. Discussion started: 14 January 2026
© Author(s) 2026. CC BY 4.0 License.

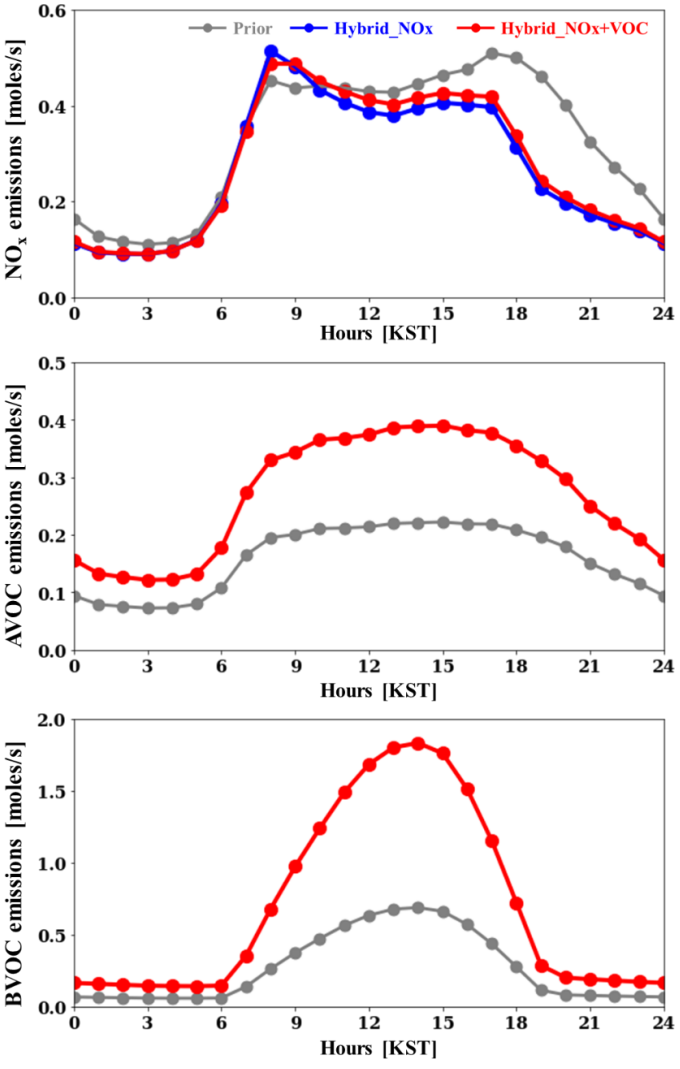

305 **Figure 6: Diurnal variations of NO_x (top), AVOC (middle), and BVOC (bottom) emissions for each experiment (Prior: gray, Hybrid_NOx: blue, Hybrid_NOx+VOC: red), averaged over South Korea during the study period.**

In summary, the Hybrid_NOx+VOC experiment led to an overall reduction in NO_x emissions and an increase in VOC emissions relative to the Prior inventory. Although NO_x emissions decreased on average, they increased during the morning
310 rush hour and decreased markedly during the evening and nighttime, indicating a shift in their temporal distribution. These results demonstrate that the proposed hybrid inverse modeling framework effectively adjusts both the spatial distribution and temporal allocation of emissions.

https://doi.org/10.5194/egusphere-2025-5837
Preprint. Discussion started: 14 January 2026
© Author(s) 2026. CC BY 4.0 License.

3.2 Spatiotemporal changes in NO_2, HCHO, and O_3 concentrations

In this section, CMAQ simulations based on the Prior, Hybrid_NOx, and Hybrid_NOx+VOC experiments were performed to assess the effectiveness of the hybrid inverse modeling approach. Before evaluating the inverse modeling performance, the meteorological fields were first validated, with the results summarized in Table S5. The model showed good agreement with observations for temperature, wind speed, and relative humidity. Subsequently, the simulated NO_2, O_3, and HCHO concentrations for each experiment were evaluated against observational data, as summarized in Table 1.

Table 1: Statistical evaluation of NO_2, HCHO, and O_3 concentrations for each experiment (Prior, Hybrid_NOx, and Hybrid_NOx+VOC). Observations of NO_2 and O_3 were obtained from the AQMS network, while HCHO observations were based on Pandora measurements.

Species	Experiment	Obs.	CMAQ	MBE	RMSE	IOA	r
NO_2 [ppb]	Prior	12.22	15.56	3.34	15.49	0.59	0.46
	Hybrid_NOx		9.00	-3.22	8.33	0.74	0.60
	Hybrid_NOx+VOC		9.41	-2.81	8.26	0.76	0.61
HCHO VCD [10^{15} molec cm^{-2}]	Prior	7.06	4.59	-2.47	4.40	0.54	0.52
	Hybrid_NOx		4.61	-2.45	4.36	0.55	0.53
	Hybrid_NOx+VOC		5.85	-1.22	3.94	0.67	0.52
O_3 [ppb]	Prior	44.48	38.20	-6.29	18.30	0.71	0.55
	Hybrid_NOx		43.74	-0.74	12.84	0.80	0.70
	Hybrid_NOx+VOC		44.72	0.24	12.34	0.83	0.73

For NO_2, the Prior experiment exhibited a positive bias, with a mean bias error (MBE) of 3.34 ppb. This overestimation was notably reduced in the Hybrid_NOx and Hybrid_NOx+VOC experiments, with MBEs of -3.22 ppb and -2.81 ppb, respectively. The temporal pattern of bias also changed: while the Prior experiment overestimated NO_2 concentrations during nighttime, both hybrid simulations substantially reduced this overprediction, resulting in concentrations closer to observations (Fig. 7). These improvements, primarily attributable to decreased nighttime NO_x emissions, led to enhanced agreement during nighttime. Consequently, the correlation coefficient (r) increased from 0.46 in the Prior experiment to above 0.6 in both hybrid experiments.

https://doi.org/10.5194/egusphere-2025-5837
Preprint. Discussion started: 14 January 2026
© Author(s) 2026. CC BY 4.0 License.

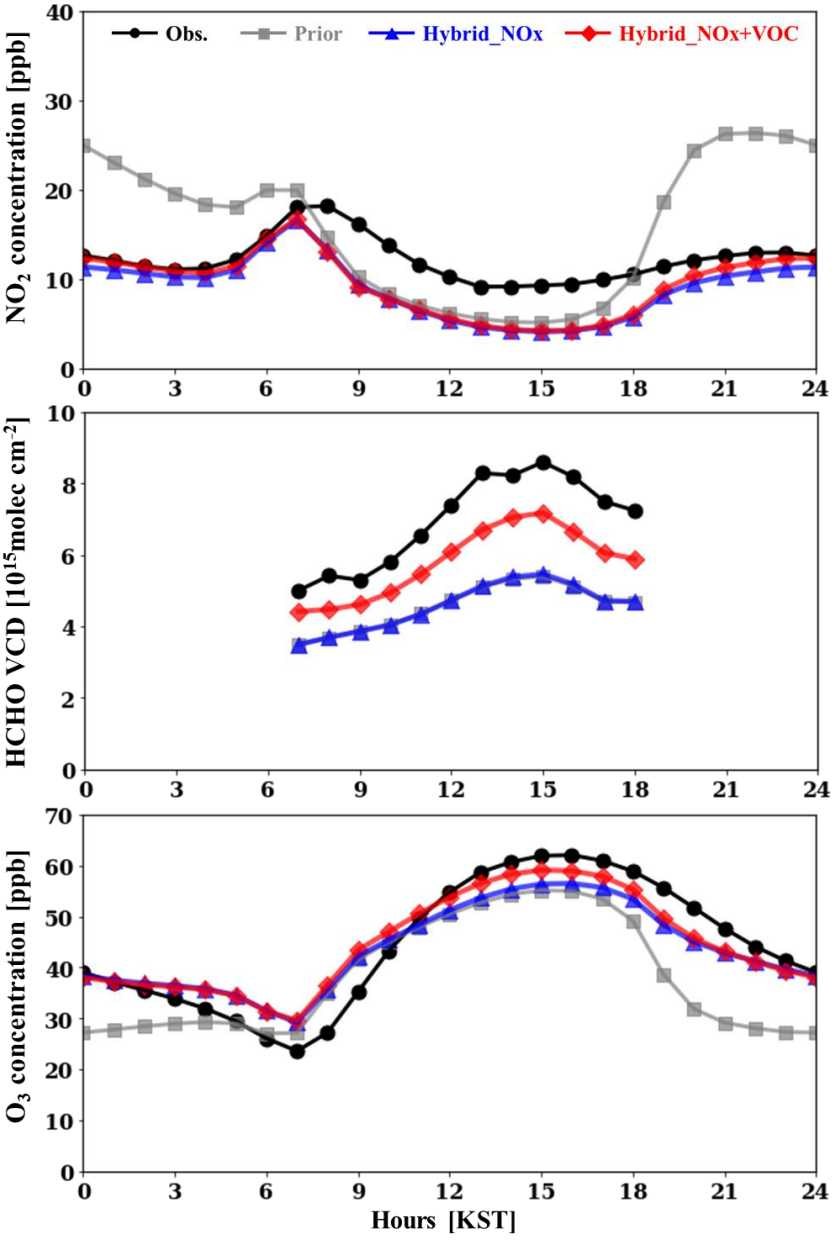

Figure 7: Diurnal variations of NO_2 (top) and O_3 (bottom) concentrations for each experiment (Prior: gray, Hybrid_NOx: blue, Hybrid_NOx+VOC: red), averaged over South Korea during the study period.

335

For VOC, model results were compared with Pandora HCHO VCDs (Table 1). The Prior experiment showed a significant underestimation (MBE = -2.48×10^{15} molec cm^{-2}). The Hybrid_NOx experiment showed little improvement (MBE = -2.45×10^{15} molec cm^{-2}), whereas the Hybrid_NOx+VOC experiment more effectively reduced the bias (MBE = -1.22×10^{15} molec cm^{-2})

https://doi.org/10.5194/egusphere-2025-5837
Preprint. Discussion started: 14 January 2026
© Author(s) 2026. CC BY 4.0 License.

and achieved the highest index of agreement (IOA = 0.67). During daytime, HCHO VCDs in both the Prior and Hybrid_NOx experiments were underestimated relative to Pandora observations, whereas the Hybrid_NOx+VOC experiment yielded higher HCHO VCDs that were closer to the Pandora measurements (Fig. 7). These results demonstrate that the underestimation of VOC emissions in the Prior experiment was effectively corrected in the Hybrid_NOx+VOC experiment, leading to improved agreement with observations across South Korea.

Regarding O_3, the Prior experiment underestimated surface concentrations, with an MBE of -6.28 ppb. The bias was substantially reduced in the Hybrid_NOx (MBE = -0.74 ppb) and Hybrid_NOx+VOC (MBE = 0.24 ppb) experiments. The IOA improved from 0.71 (Prior) to 0.80 (Hybrid_NOx) and 0.83 (Hybrid_NOx+VOC), indicating enhanced model performance in reproducing observed O_3 concentrations. In terms of diurnal variation, the Prior experiment generally underestimated O_3 with particularly large negative biases at night. In the Hybrid_NOx experiment, nighttime O_3 concentrations increased markedly, although daytime changes were limited. By contrast, the Hybrid_NOx+VOC experiment increased O_3 concentrations during both daytime and nighttime, yielding the closest agreement with observations. Spatially, the Prior experiment substantially underestimated O_3 concentrations in urban areas with high NO_x emissions, whereas the Hybrid_NOx+VOC experiment produced higher O_3 levels in these regions, resulting in improved agreement with the observations (Fig. 8).

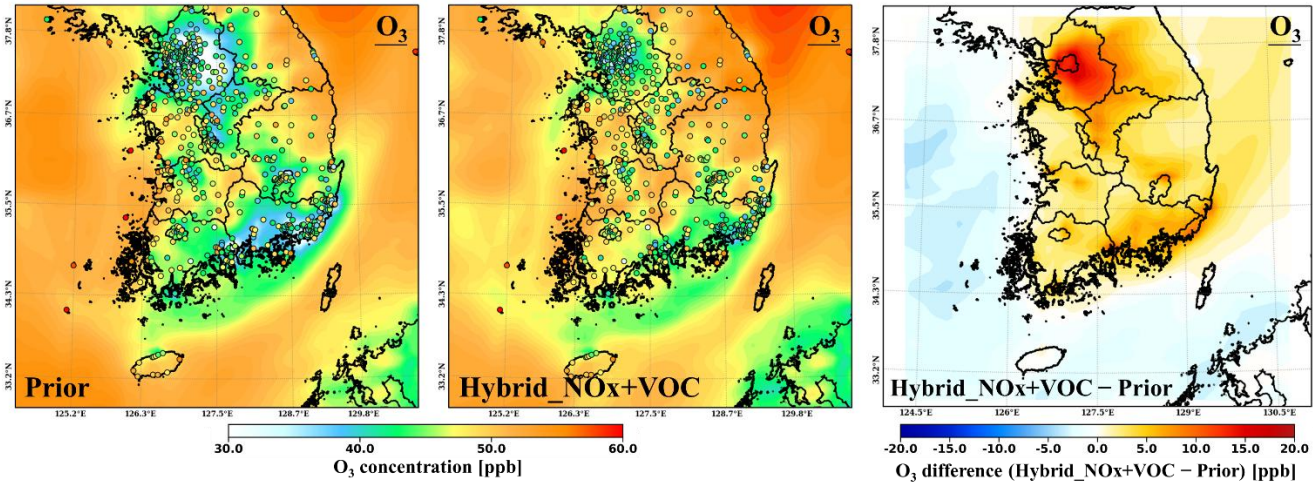

Figure 8: Spatial distributions of mean surface O_3 concentrations from the Prior (left) and Hybrid_NOx+VOC (middle) experiments, and the differences (Hybrid_NOx+VOC - Prior; right), averaged over the study period. Circles indicate O_3 observations from the AQMS network.

Consequently, the titration of O_3 by NO during nighttime was reduced, leading to increased O_3 concentrations that were more consistent with observations. However, daytime O_3 levels remained similar to those in the Prior experiment. In contrast, the Hybrid_NOx+VOC experiment significantly improved O_3 simulations during both daytime and nighttime. These findings

https://doi.org/10.5194/egusphere-2025-5837
Preprint. Discussion started: 14 January 2026
© Author(s) 2026. CC BY 4.0 License.

demonstrate that jointly constraining NO_x and VOC emissions is more effective than constraining NO_x alone in accurately reproducing O_3 concentrations over South Korea.

3.3 Improvement of O_3 sensitivity regimes through hybrid inversion

In this section, we examine how the O_3 sensitivity regime changes before and after the application of the hybrid inverse modeling. The O_3 sensitivity is diagnosed using the FNR. Figure 9 compares the FNR distributions derived from TROPOMI with those simulated in the Hybrid_NOx+VOC experiment. The TROPOMI-based FNR indicates VOC-sensitive regimes over major urban regions such as the SMA, Busan, Ulsan, and Daegu, whereas NO_x-sensitive regimes dominate over mountainous and heavily vegetated areas where BVOC emissions are substantial.

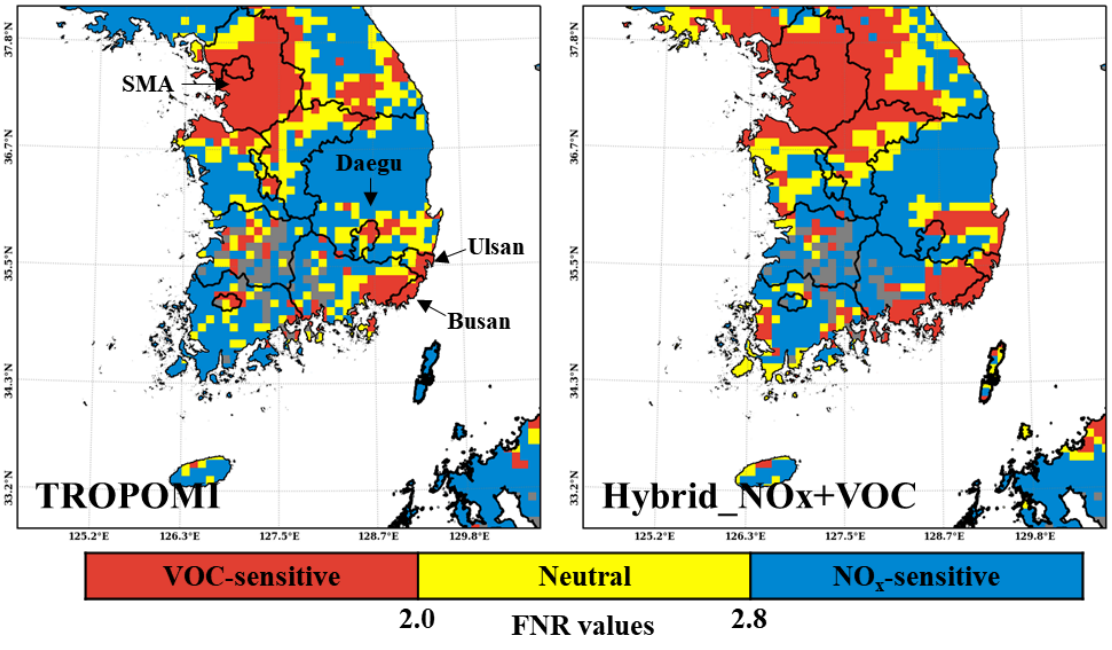

Figure 9: Spatial distributions of O_3 sensitivity regimes derived from TROPOMI-based FNR (left), and Hybrid_NOx+VOC experiments (right), averaged over the study period. Red, yellow, and blue denote VOC-sensitive, neutral, and NO_x-sensitive regimes, respectively, while gray areas indicate missing data.

The Hybrid_NOx+VOC experiment successfully reproduces the spatial pattern of the TROPOMI-based FNR, in sharp contrast to the Prior and Hybrid_NOx experiments, which classify most of South Korea as VOC-sensitive (Fig. S3). The Prior emissions are based on the 2018 EDGAR HTAPv3 inventory, whose earlier base year may not fully reflect emission conditions in 2022, potentially biasing the Prior experiment toward VOC-sensitive regimes. Furthermore, adjusting NO_x emissions alone

https://doi.org/10.5194/egusphere-2025-5837
Preprint. Discussion started: 14 January 2026
© Author(s) 2026. CC BY 4.0 License.

in the Hybrid_NOx experiment was insufficient to capture the observed O_3 sensitivity regime, indicating that simultaneous optimization of both NO_x and VOC emissions is essential for accurately diagnosing O_3 chemical regimes.

The improved agreement in the Hybrid_NOx+VOC experiment highlights the importance of integrating recent satellite observations into emission updates, enabling the model to better reflect the current photochemical environment. These findings are consistent with recent studies reporting regional transitions in East Asia from VOC-sensitive toward NO_x-sensitive or transitional regimes (Lee et al., 2021; Itahashi et al., 2022; Wang et al., 2025).

Given that the hybrid inversion yields O_3 sensitivity regimes that closely resemble those derived from TROPOMI, the optimized posterior state provides a robust foundation for further analysis. Accordingly, in Section 3.4, we assess the regime-dependent hourly ΔO_3 responses to NO_x and VOC emissions using adjoint sensitivities derived from the posterior simulation.

3.4 Regime-dependent hourly ΔO_3 responses to NO_x and VOC emissions

We quantify hourly ΔO_3 responses using adjoint sensitivities to determine, within VOC-sensitive and NO_x-sensitive regimes, which precursor (NO_x or VOC) exerts a stronger influence on O_3 production or loss. Figure 10 shows regime-stratified hourly ΔO_3 responses to NO_x and VOC emissions for 1–14 May 2022. Panels (a) and (c) show, for each local hour, the ΔO_3 at that hour resulting from emissions integrated over all emission times (Eq. (12)). This reflects not only the response to emissions released at the same hour but also the influence of the full diurnal emission profile of each precursor on hourly O_3. Thus, the panels illustrate how the complete daily emission cycle of each precursor contributes to hourly O_3 within each regime.

In the VOC-sensitive regime (NO_x-rich), the NO_x response is negative at all hours, indicating net O_3 decreases consistent with rapid O_3 titration, whereas the VOC response is positive and strengthens during daytime, reflecting enhanced photochemical production. In the NO_x-sensitive regime (VOC-rich), VOC provides a persistent positive daytime response, while the NO_x response changes sign with time of day: negative at night (titration) and positive from late morning into the afternoon as radical chemistry intensifies.

https://doi.org/10.5194/egusphere-2025-5837
Preprint. Discussion started: 14 January 2026
© Author(s) 2026. CC BY 4.0 License.

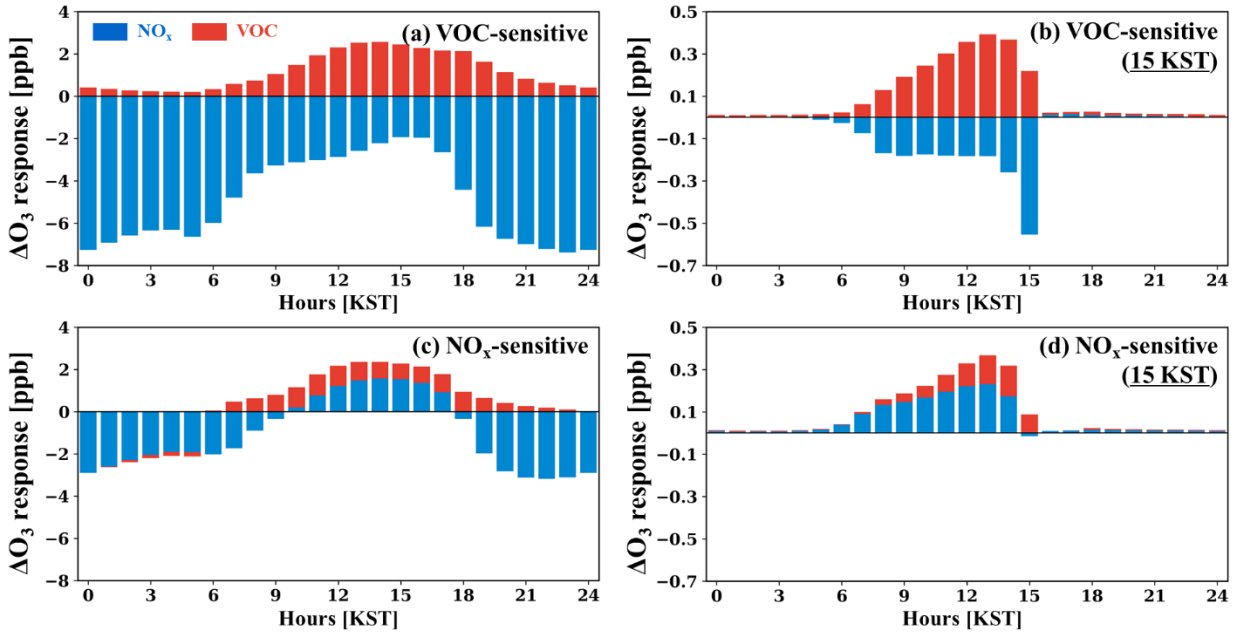

Figure 10: Two-week mean ΔO_3 response (ppb) to NO_x (blue) and VOC (red) emissions, by local hour, for 1–14 May 2022. For each local hour, responses are summed over all grids classified in each regime at that hour; regimes are diagnosed with the FNR indicator from the Hybrid_NOx+VOC experiment. Panels (a) and (c) show, for VOC-sensitive and NO_x-sensitive regimes respectively, the ΔO_3 response at each local hour to emissions released over all hours (i.e., emission-time–integrated response). Panels (b) and (d) show the ΔO_3 response at 15 KST as a function of emission time ("emission-time response").

Panels (b) and (d) isolate the hour of maximum O_3 (15 KST) and display the ΔO_3 response at 15 KST as a function of the emission time (Eq. (11)). In VOC-sensitive regimes, NO_x emitted at 15 KST yields the largest negative ΔO_3 response, consistent with the instantaneous O_3 titration. By contrast, VOC emissions at 13 KST exert the strongest positive influence on 15 KST O_3, indicating an effective lag of about 2 hours associated with multistep photochemical production. In NO_x-sensitive regimes, NO_x generally promotes O_3 formation; however, NO_x emitted at 15 KST still produces O_3 losses through immediate titration. The largest positive effects on 15 KST O_3 arise from NO_x at 13 KST and VOC at 14 KST, indicating a similar response time of approximately 1–2 hours.

Taken together, the results show that precursor impacts on O_3 vary with both regime and hour. Under VOC-sensitive conditions, VOC reductions are more effective than NO_x reductions for lowering daytime O_3, whereas under NO_x-sensitive conditions, NO_x controls deliver the more direct decreases. Because titration is immediate but photochemical production requires chemical processing time, effective mitigation of high-O_3 periods requires hour-specific emission controls aligned with the prevailing O_3 sensitivity regime.

A clear understanding of how precursor influences on O_3 differ across sensitivity regimes and vary throughout the day is essential for designing realistic and region-specific O_3 control strategies. In this context, the hybrid inversion framework presented in this study provides a practical basis for policy development, as it enables accurate identification of the dominant

https://doi.org/10.5194/egusphere-2025-5837
Preprint. Discussion started: 14 January 2026
© Author(s) 2026. CC BY 4.0 License.

O_3 sensitivity regime and quantification of the major precursor contributions. By capturing both the chemical regime and the temporal characteristics of precursor impacts, the proposed methodology can provide valuable guidance for developing region-specific and effective emission reduction strategies.

This analysis is limited to a two-week period and may not capture the seasonal or longer-term variability of O_3 sensitivity regimes across South Korea. Nevertheless, the hybrid inverse modeling framework efficiently constrains precursor emissions on short time scales and enables assessments tailored to individual regions that explicitly account for the prevailing O_3 sensitivity regime, thereby supporting the implementation of emission reduction policies. Compared with conventional bottom-up inventories, the top-down approach reduces data and computational demands, enables rapid observation-driven estimates of O_3 precursor emissions, and provides timely guidance for O_3 management policies.

4. Summary and Conclusions

This study aimed to enhance the accuracy of simulated O_3 concentrations and improve the diagnosis of O_3 sensitivity regimes over South Korea by applying a top-down hybrid inverse modeling approach to constrain the spatiotemporal distributions of NO_x and VOC emissions, and to quantify hourly ΔO_3 responses to these precursors using adjoint sensitivities. The inverse modeling system used TROPOMI NO_2 and HCHO column densities along with surface NO_2 and O_3 measurements from the AQMS network. The modeling was conducted using CMAQ and its adjoint model. The hybrid inverse modeling approach combining the FDMB and 4D-Var methods was employed to constrain emissions. To assess the impact of major O_3 precursors on the spatiotemporal distribution and sensitivity regime of O_3, three experiments were conducted: Prior, which used the EDGAR_HTAPv3 emission inventory; Hybrid_NOx, in which only NO_x emissions were optimized; and Hybrid_NOx+VOC, in which both NO_x and VOC emissions were jointly constrained.

In the Hybrid_NOx experiment, where only NO_x emissions were adjusted, emissions decreased by up to 51 % at night and increased by up to 14 % during the day relative to the Prior inventory, resulting in an overall average reduction of 18 %. These time-dependent adjustments enabled the correction of diurnal variability in the emission profile. Consequently, nighttime O_3 concentrations increased, reducing the mean bias error by 90 % relative to the Prior experiment and thereby improving agreement with observations. In contrast, during the daytime, constraining NO_x emissions alone yielded only limited improvements in O_3 concentrations.

However, constraining NO_x alone provided only limited improvement for daytime O_3, indicating the need to additionally optimize VOC emissions. To address this limitation, the Hybrid_NOx+VOC experiment was conducted, in which both NO_x and VOC emissions were simultaneously constrained. Compared to the Prior emissions, NO_x decreased by an average of 16 %, while anthropogenic AVOC and BVOC increased by 71 % and 162 %, respectively. The joint adjustment of NO_x and VOC emissions yielded the greatest improvement in O_3 simulations during both daytime and nighttime, resulting in an IOA exceeding 0.8 when compared with AQMS O_3 observations. These results demonstrate that accurate O_3 simulation requires the simultaneous constraint of NO_x and VOC emissions due to nonlinear chemical processes. Furthermore, given the

https://doi.org/10.5194/egusphere-2025-5837
Preprint. Discussion started: 14 January 2026
© Author(s) 2026. CC BY 4.0 License.

substantial differences in photochemical mechanisms between day and night, accurately representing not only the spatial distribution but also the diurnal variability of emissions is critical for improving O_3 model performance.

The hybrid inverse modeling also improved the simulation of O_3 sensitivity regimes. In the Hybrid_NOx+VOC experiment, the spatial distribution of the simulated FNR closely matched the TROPOMI-derived regimes, reproducing VOC-sensitive conditions over major urban regions and NO_x-sensitive conditions over mountainous and vegetated areas. This agreement highlights the ability of the hybrid inversion to incorporate observational constraints and accurately represent the relative contributions of NO_x and VOC to O_3 formation. The improved regime classification further provides a reliable foundation for analyzing regime-dependent O_3 production and understanding how changes in precursor abundances drive transitions between VOC-sensitive and NO_x-sensitive conditions.

Building on the improved regime representation obtained from the Hybrid_NOx+VOC experiment, we further analyzed how each precursor influences O_3 in a regime- and time-dependent manner. Under VOC-sensitive conditions, VOC emissions sustain daytime O_3 production, whereas NO_x emissions lead to net O_3 losses through rapid titration. In contrast, under NO_x-sensitive conditions, NO_x contributes positively to O_3 formation from late morning into the afternoon, while titration processes dominate during nighttime hours. These results clarify precursor-specific emission control priorities with explicit diurnal dependence: in VOC-sensitive regimes, reducing VOC emissions is most effective for mitigating daytime O_3, whereas in NO_x-sensitive regimes, NO_x emission reductions provide more immediate and direct benefits. Because titration occurs almost instantaneously while photochemical production unfolds over finite chemical timescales, effective mitigation of high-O_3 periods requires hour-specific emission controls that are aligned with the prevailing O_3 sensitivity regime.

This analysis spans two weeks and therefore may not capture seasonal or long-term variability. In addition, because EDGAR_HTAPv3 was spatiotemporally downscaled for CMAQ, inventory-related uncertainties could not be fully assessed. Despite these limitations, the findings suggest that extending the hybrid inverse modeling over longer periods and incorporating diverse observations would further improve the resolution and reliability of emission estimates. Overall, the proposed hybrid inverse modeling shows strong potential to enhance O_3 simulations and to support region-specific regime assessments and precursor emission control strategies.

Code and data availability. The WRF 3.8.1 model is distributed by NCAR (https://www.mmm.ucar.edu/models/wrf, last access: 21 November 2025; Skamarock et al., 2008). The CMAQ 5.0 adjoint model is available from Zenodo (https://zenodo.org/records/3780216, last access: 21 November 2025; Zhao et al., 2020). The MEGAN 2.1 model is available from the University of California, Irvine – Biogenic Aerosols and Interactions Research Group (BAI) (https://bai.ess.uci.edu/megan/data-and-code/megan21, last access: 21 November 2025; Guenther et al., 2012). ERA5 reanalysis data are distributed by the Climate Data Store of ECMWF (https://cds.climate.copernicus.eu/datasets, last access: 21 November 2025; Hersbach et al., 2023a, b). The EDGAR HTAPv3 emission inventory is provided by the European Commission Joint Research Centre (https://edgar.jrc.ec.europa.eu/dataset_htap_v3, last access: 21 November 2025; Crippa et

https://doi.org/10.5194/egusphere-2025-5837
Preprint. Discussion started: 14 January 2026
© Author(s) 2026. CC BY 4.0 License.

al., 2023). TROPOMI NO_2 and HCHO column data are available from the Copernicus Data Space (https://dataspace.copernicus.eu, last access: 21 November 2025). Pandora HCHO column data are accessible from the Pandonia Global Network (https://www.pandonia-global-network.org, last access: 21 November 2025). AQMS NO_2 and O_3 observations are available from AirKorea (https://www.airkorea.or.kr/web, last access: 21 November 2025).

Author contributions. JM designed and executed the model inversions, performed the data analysis, and prepared the manuscript. WJ, YC, HCK, and SYP provided scientific and technical guidance and contributed to the scientific analysis and interpretation of the results. WJ and SJ were responsible for funding acquisition. All authors contributed to the review and editing of the final paper.

Competing interests. The contact author has declared that none of the authors has any competing interests.

Acknowledgments. This study is based in part on the doctoral dissertation of the first author. This research was supported by Korea Environmental Industry & Technology Institute (KEITI) through "Project for developing an observation-based GHG emissions geospatial information map", funded by Korea Ministry of Environment (MOE) (RS-2023-00232066) and the National Research Foundation of Korea (NRF) grant funded by the Korea Government (MSIT) (No. RS-2023-NR076349). The work by H.C.K was partly supported by NOAA grant NA24NESX432C0001 (CISESS).

References

Bae, K., Song, C.K., Van Roozendael, M., Richter, A., Wagner, T., Merlaud, A., Pinardi, G., Friedrich, M.M., Fayt, C., Dimitropoulou, E., Lange, K., and Bösch, T., Zilker, B., Latsch, M., Behrens, L.K., Ziegler, S., Ripperger-Lukosiunaite, S., Kuhn, L., Lauster, B., Reischmann, L., Uhlmannsiek, K., Cede, A., Tiefengraber, M., Gebetsberger, M., Park, R.J., Lee, H., Hong, H., Chang, L.S., Jeon, K. Validation of GEMS operational v2.0 total column NO_2 and HCHO during the GMAP/SIJAQ campaign. Sci. Total Environ. 974 (2), 179190, https://doi.org/10.1016/j.scitotenv.2025.179190, 2025.

Chen, Y., Shen, H., Kaiser, J., Hu, Y., Capps, S.L., Zhao, S., Hakami, A., Shih, J.-S., Pavur, G.K., Turner, M.D., Henze, D.K., Resler, J., Nenes, A., Napelenok, S.L., Bash, J.O., Fahey, K.M., Carmichael, G.R., Chai, T., Clarisse, L., Coheur, P.-F., van Damme, M., Russell, A.G.: High-resolution hybrid inversion of IASI ammonia columns to constrain US ammonia emissions using the CMAQ adjoint model, Atmos. Chem. Phys., 21, 2067–2082, https://doi.org/10.5194/acp-21-2067-2021, 2021.

Cheng, X., Hao, Z., Zang, Z., Liu, Z., Xu, X., Wang, S., Liu, Y., Hu, Y., Ma, X.: A new inverse modeling approach for emission sources based on the DDM-3D and 3DVAR techniques: an application to air quality forecasts in the Beijing-Tianjin-Hebei region, Atmos. Chem. Phys., 21 (18), 13747–13761, https://doi.org/10.5194/acp- 21-13747-2021, 2021.

https://doi.org/10.5194/egusphere-2025-5837
Preprint. Discussion started: 14 January 2026
© Author(s) 2026. CC BY 4.0 License.

Choi, J., Henze, D. K., Cao, H., Nowlan, C. R., González Abad, G., Kwon, H.-A., Lee, H.-M., Oak, Y. J., Park, R. J., Bates, K. H., Maasakkers, J. D., Wisthaler, A., and Weinheimer, A. J.: An inversion framework for optimizing nonmethane VOC emissions using remote sensing and airborne observations in northeast Asia during the KORUS-AQ field campaign, J. Geophys. Res.-Atmos., 127, e2021JD035844, https://doi.org/10.1029/2021JD035844, 2022.

Cooper, M.J., Martin, R.V., Henze, D.K., Jones, D.B.A.: Effects of a priori profile shape assumptions on comparisons between satellite NO_2 columns and model simulations, Atmos. Chem. Phys., 20, 7231–7241, https://doi.org/10.5194/acp-20- 7231-2020, 2020.

Cooper, M., Martin, R.V., Padmanabhan, A., Henze, D.K.: Comparing mass balance and adjoint methods for inverse modeling of nitrogen dioxide columns for global nitrogen oxide emissions., J. Geophys. Res.-Atmos., 122, 4718–4734, https://doi.org/10.1002/2016JD025985, 2017.

Crippa, M., Guizzardi, D., Butler, T., Keating, T., Wu, R., Kaminski, J., Kuenen, J., Kurokawa, J., Chatani, S., Morikawa, T., Pouliot, G., Racine, J., Moran, M.D., Klimont, Z., Manseau, P.M., Mashayekhi, R., Henderson, B.H., Smith, S.J., Suchyta, H., Muntean, M., Solazzo, E., Banja, M., Schaaf, E., Pagani, F., Woo, J.-H., Kim, J., Monforti-Ferrario, F., Pisoni, E., Zhang, J., Niemi, D., Sassi, M., Ansari, T., Foley, K.: The HTAP_v3 Emission Mosaic: Merging Regional and Global Monthly Emissions (2000–2018) to Support Air Quality Modelling and Policies, Earth Syst. Sci. Data, 15 (6), 2667–2694, https://doi.org/10.5194/essd-15-2667-2023, 2023.

Crippa, M., Solazzo, E., Huang, G., Guizzardi, D., Koffi, E., Muntean, M., Schieberle, C., Friedrich, R., Janssens-Maenhout, G.: High resolution temporal profiles in the Emissions Database for Global Atmospheric Research, Sci. Data, 7 (1), 121, http://dx.doi.org/10.1038/s41597- 020-0462-2, 2020.

De Smedt, I., Pinardi, G., Vigouroux, C., Compernolle, S., Bais, A., Benavent, N., Boersma, F., Chan, K.L., Donner, S., Eichmann, K.U., Hedelt, P., Hendrick, F., Irie, H., Kumar, V., Lambert, J.C., Langerock, B., Lerot, C., Liu, C., Loyola, D., Piters, A., Richter, A., Rivera Cárdenas, C., Romahn, F., Ryan, R.G., Sinha, V., Theys, N., Vlietinck, J., Wagner, T., Wang, T., Yu, H., Van Roozendael, M.: Comparative assessment of TROPOMI and OMI formaldehyde observations and validation against MAX-DOAS network column measurements, Atmos. Chem. Phys., 21, 12561–12593, https://doi.org/10.5194/ACP-21-12561- 2021, 2021.

Douros, J., Eskes, H., van Geffen, J., Boersma, K. F., Compernolle, S., Pinardi, G., Blechschmidt, A.-M., Peuch, V.-H., Colette, A., Veefkind, P.: Comparing Sentinel-5P TROPOMI NO_2 column observations with the CAMS regional air quality ensemble, Geosci. Model Dev., 16, 509–534, https://doi.org/10.5194/gmd-16-509-2023, 2023.

Duncan, B.N., Yoshida, Y., Olson, J.R., Sillman, S., Martin, R.V., Lamsal, L., Hu, Y., Pickering, K.E., Retscher, C., Allen, D.J., Crawford, J.H.: Application of OMI observations to a space-based indicator of NO_x and VOC controls on surface ozone formation, Atmos. Environ., 44 (18), 2213–2223, https://doi.org/10.1016/j.atmosenv.2010.03.010, 2010.

East, J.D., Henderson, B.H., Napelenok, S.L., Koplitz, S.N., Sarwar, G., Gilliam, R., Lenzen, A., Tong, D.Q., Pierce, R.B., Garcia-Menendez, F.: Inferring and evaluating satellite-based constraints on NO_x emissions estimates in air quality simulations, Atmos. Chem. Phys., 22, 15981–16001, https:// doi.org/10.5194/acp-22-15981-2022, 2022.

https://doi.org/10.5194/egusphere-2025-5837
Preprint. Discussion started: 14 January 2026
© Author(s) 2026. CC BY 4.0 License.

Elbern, H., Strunk, A., Schmidt, H., Talagrand, O.: Emission rate and chemical state estimation by 4-dimensional variational inversion, Atmos. Chem. Phys., 7 (14), 3749–3769, https://doi.org/10.5194/acp-7-3749-2007, 2007.

Feng, S., Jiang, F., Jiang, Z., Wang, H., Cai, Z., Zhang, L.: Impact of 3DVAR assimilation of surface $PM_{2.5}$ observations on $PM_{2.5}$ forecasts over China during wintertime, Atmos. Environ., 187, 34-49, https://doi.org/10.1016/j.atmosenv.2018.05.049, 2018.

Fu, W., Zhu, L., Kwon, H. A., Park, R. J., Lee, G. T., De Smedt, I., Liu, S., Li, X., Chen, Y., Pu, D., Li, J., Zuo, X., Zhang, P., Li, Y., Yan, Z., Zhang, X., Zhang, J., Wu, X., Shen, H., Ye, J., Wang, C., Fu, T.-M., Yang, X.: Evaluating GEMS HCHO retrievals with TROPOMI product, Pandora observations, and GEOS-Chem simulations, Earth Space Sci., 12, https://doi.org/10.1029/2024EA003894, 2025.

Goldberg, D.L., Tao, M., Kerr, G.H., Ma, S., Tong, D., Fiore, A.M., Dickens, A.F., Adelman, Z., Anenberg, S.C.: Evaluating the spatial patterns of U.S. urban NO_x emissions using TROPOMI NO_2, Remote Sens. Environ., 300, 113917, https://doi.org/10.1016/j.rse.2023.113917, 2024.

Gryparis, A., Forsberg, B., Katsouyanni, K., Analitis, A., Touloumi, G., Schwartz, J., Samoli, E., Medina, S., Anderson, H.R., Niciu, E.M., Wichmann, H.E., Kriz, B., Kosnik, M., Skorkovsky, J., Vonk, J.M., Dörtbudak, Z.: Acute effects of ozone on mortality from the "Air Pollution and Health: A European Approach" project, Am. J. Respir. Crit. Care Med., 170, 1080–1087, https://doi.org/10.1164/rccm.200403-333OC, 2004.

Guenther, A.B., Jiang, X., Heald, C.L., Sakulyanontvittaya, T., Duhl, T., Emmons, L.K., Wang, X.: The model of emissions of gases and aerosols from Nature version 2.1 (MEGAN2.1): an extended and updated framework for modeling biogenic emissions, Geosci. Model Dev., 5, 1471–1492, https://doi.org/10.5194/gmd-5-1471-2012, 2012.

Hansen, P. C.: The L-curve and its use in the numerical treatment of inverse problems, IMM Tech. Rep. 15/1999, Kongens Lyngby, Denmark, 1999.

Henze, D. K., Seinfeld, J. H., Shindell, D. T.: Inverse modeling and mapping US air quality influences of inorganic $PM_{2.5}$ precursor emissions using the adjoint of GEOS-Chem, Atmos. Chem. Phys., 9, 5877-5903, https://doi.org/10.5194/acp-9-5877-2009, 2009.

Hersbach, H., Bell, B., Berrisford, P., Biavati, G., Horányi, A., Muñoz Sabater, J., Nicolas, J., Peubey, C., Radu, R., Rozum, I., Schepers, D., Simmons, A., Soci, C., Dee, D., Thépaut, J-N.: ERA5 hourly data on pressure levels from 1940 to present. Copernicus Climate Change Service (C3S) Climate Data Store (CDS), https://doi.org/10.24381/cds.bd0915c6 (Accessed on 12-Sep-2025), 2023a.

Hersbach, H., Bell, B., Berrisford, P., Biavati, G., Horányii, A., Muñoz Sabater, J., Nicolas, J., Peubey, C., Radu, R., Rozum, I., Schepers, D., Simmons, A., Soci, C., Dee, D., and Thépaut, J.-N.: ERA5 hourly data on pressure levels from 1940 to present, Copernicus Climate Change Service (C3S) Climate Data Store (CDS), https://doi.org/10.24381/cds.adbb2d47 (Accessed on 12-Sep-2025), 2023b.

Hou, X., Wild, O., Zhu, B., Lee, J.: Future tropospheric ozone budget and distribution over east Asia under a net-zero scenario, Atmos. Chem. Phys., 23, 15395–15411, https://doi.org/10.5194/acp-23-15395-2023, 2023.

https://doi.org/10.5194/egusphere-2025-5837
Preprint. Discussion started: 14 January 2026
© Author(s) 2026. CC BY 4.0 License.

Hristov, A.N., Harper, M., Meinen, R., Day, R., Lopes, J., Ott, T., Venkatesh, A., Randles, C.A.: Discrepancies and Uncertainties in Bottom-up Gridded Inventories of Livestock Methane Emissions for the Contiguous United States, Environ. Sci. Technol., 51, 13668–13677, https://doi.org/10.1021/acs.est.7b03332, 2017.

Hu, Y., Li, Y., Ma, X., Liang, Y., You, W., Pan, X., Zang, Z.: The optimization of SO_2 emissions by the 4DVAR and EnKF methods and its application in WRF-Chem, Sci. Total Environ., 888, 163796, https://doi.org/10.1016/j.scitotenv.2023.163796, 2023.

Hu, Y., Zang, Z., Ma, X., Li, Y., Liang, Y., You, W., Pan, X., Li, Z.: Four-dimensional variational assimilation for SO_2 emission and its application around the COVID-19 lockdown in the spring 2020 over China, Atmos. Chem. Phys., 22, 13183–13200, https://doi.org/10.5194/acp-22-13183-2022, 2022.

Itahashi, S., Irie, H., Shimadera, H., Chatani, S.: Fifteen-year trends (2005–2019) in the satellite-derived ozone-sensitive regime in East Asia: a gradual shift from VOC-Sensitive to NO_x-Sensitive, Remote Sens., 14, https://doi.org/10.3390/rs14184512, 2022.

Jang, J., Lee, Y. G., Yu, J. A., Sung, K. H., Kim, S. M.: Characteristic Analysis of Tropospheric Ozone Sensitivity from the Satellite-Based $HCHO/NO_2$ Ratio in South Korea, Korean J. Remote Sens., 39 (5–1), 563–576, https://doi.org/10.7780/kjrs.2023.39.5.1.8, 2023.

Jeon, W., Choi, Y., Lee, H.W., Lee, S.H., Yoo, J.W., Park, J., Lee, H.J.: A quantitative analysis of grid nudging effect on each process of $PM_{2.5}$ production in the Korean Peninsula, Atmos. Environ., 122, 763–774, https://doi.org/10.1016/j.atmosenv.2015.10.050, 2015.

Jia, G., Huang, Z., Tang, X., Ou, J., Lu, M., Xu, Y., Zhong, Z., Sha, Q., Wu, H., Zheng, C., Deng, T., Chen, D., He, M., Zheng, J.: A meteorologically adjusted ensemble Kalman filter approach for inversing daily emissions: a case study in the Pearl River Delta, China, J. Environ. Sci., 114, 233–248, https://doi.org/10.1016/j.jes.2021.08.048, 2022.

Judd, L. M., Al-Saadi, J. A., Szykman, J. J., Valin, L. C., Janz, S. J., Kowalewski, M. G., Eskes, H. J., Veefkind, J. P., Cede, A., Mueller, M., Gebetsberger, M., Swap, R., Pierce, R. B., Nowlan, C. R., Abad, G. G., Nehrir, A., Williams, D.: Evaluating sentinel-5P TROPOMI tropospheric NO_2 column densities with airborne and Pandora spectrometers near New York City and Long Island sound, Atmos. Meas. Tech., 13 (11), 6113–6140, https://doi.org/10.5194/amt-13-6113-2020, 2020.

Lamsal, L.N., Martin, R.v., Padmanabhan, A., van Donkelaar, A., Zhang, Q., Sioris, C.E., Chance, K., Kurosu, T.P., Newchurch, M.J.: Application of satellite observations for timely updates to global anthropogenic NO_x emission inventories, Geophys. Res. Lett., 38, L05810, https://doi.org/10.1029/2010GL046476, 2011.

Lee, H.J., Chang, L.S., Jaffe, D.A., Bak, J., Liu, X., Abad, G.G., Jo, H.-Y., Jo, Y.-J., Lee, J.-B., Kim, C.-H.: Ozone continues to increase in East Asia despite decreasing NO_2: Causes and abatements, Remote Sens., 13, 2177, https://doi.org/10.3390/rs13112177, 2021.

Li, C., Martin, R.V., Shephard, M.W., Cady-Pereira, K., Cooper, M.J., Kaiser, J., Lee, C.J., Zhang, L., Henze, D.K.: Assessing the iterative finite difference mass balance and 4D-Var methods to derive ammonia emissions over North America using synthetic observations, J. Geophys. Res.-Atmos., 124, 4222–4236, https://doi.org/ 10.1029/2018JD030183, 2019.

https://doi.org/10.5194/egusphere-2025-5837
Preprint. Discussion started: 14 January 2026
© Author(s) 2026. CC BY 4.0 License.

Liu, J., Li, X., Tan, Z., Wang, W., Yang, Y., Zhu, Y., Yang, S., Song, M., Chen, S., Wang, H., Lu, K., Zeng, L., Zhang, Y.: Assessing the Ratios of Formaldehyde and Glyoxal to NO_2 as Indicators of O_3-NO_x-VOC Sensitivity, Environ. Sci. Technol., 55, 10935-10945, https://doi.org/10.1021/acs.est.0c07506, 2021.

Liu, C., Shi, K.: A review on methodology in O_3-NO_x-VOC sensitivity study, Environ. Pollut., 291, 118249, https://doi.org/10.1016/j.envpol.2021.118249, 2021.

Millet, D. B., Jacob, D. J., Turquety, S., Hudman, R. C., Wu, S., Fried, A., Walega, J., Heikes, B. G., Blake, D. R., Singh, H. B., Anderson, B. E., Clarke, A. D.: Formaldehyde distribution over North America: Implications for satellite retrievals of formaldehyde columns and isoprene emission, J. Geophys. Res.-Atmos., 111, D24S02, doi:10.1029/2005JD006853, 2006.

Miller, S.M., Michalak, A.M., Levi, P.J.: Atmospheric inverse modeling with known physical bounds: an example from trace gas emissions, Geosci. Model Dev., 7, 303-315, https://doi.org/10.5194/gmd-7-303-2014, 2014.

Momeni, M., Choi, Y., Yeganeh, A.K., Pouyaei, A., Jung, J., Park, J., Shephard, M.W., Dammers, E., Cady-Pereira, K.E.: Constraining East Asia ammonia emissions through satellite observations and iterative Finite Difference Mass Balance (iFDMB) and investigating its impact on inorganic fine particulate matter, Environ. Int., 184, 108473, https://doi.org/10.1016/j.envint.2024.108473, 2023.

Moon, J., Choi, Y., Jeon, W., Kim, H.C., Pouyaei, A., Jung, J., Pan, S., Kim, S., Kim, C.-H., Bak, J., Yoo, J.-W., Park, J., Kim, D.: Hybrid IFDMB/4D-Var inverse modeling to constrain the spatiotemporal distribution of CO and NO_2 emissions using the CMAQ adjoint model, Atmos. Environ., 327, 120490, https://doi.org/10.1016/j.atmosenv.2024.120490, 2024.

Mun, J., Choi, Y., Jeon, W., Lee, H.W., Kim, C.-H., Park, S.-Y., Bak, J., Jung, J., Oh, I., Park, J., Kim, D.: Assessing mass balance-based inverse modeling methods via a pseudo-observation test to constrain NO_x emissions over South Korea, Atmos. Environ., 292, 119429, https://doi.org/10.1016/j.atmosenv.2022.119429, 2023.

Oomen, G.-M., Müller, J.-F., Stavrakou, T., De Smedt, I., Blumenstock, T., Kivi, R., Makarova, M., Palm, M., Röhling, A., Té, Y., Vigouroux, C., Friedrich, M. M., Frieß, U., Hendrick, F., Merlaud, A., Piters, A., Richter, A., Van Roozendael, M., Wagner, T.: Weekly derived top-down volatileorganic-compound fluxes over Europe from TROPOMI HCHO data from 2018 to 2021, Atmos. Chem. Phys., 24, 449–474, https://doi.org/10.5194/acp-24-449-2024, 2024.

Peng, Z., Liu, Z., Chen, D., Ban, J.: Improving $PM_{2.5}$ forecast over China by the joint adjustment of initial conditions and source emissions with an ensemble Kalman filter, Atmos. Chem. Phys., 17, 4837–4855, https://doi.org/10.5194/acp-17-4837-2017, 2017.

Qu, Z., Henze, D.K., Theys, N., Wang, J., Wang, W.: Hybrid Mass balance/4D-var joint inversion of NO_x and SO_2 emissions in East Asia, J. Geophys. Res.-Atmos., 124, 8203–8224. https://doi.org/10.1029/2018JD030240, 2019.

Rahman, M.M., Shults, R., Ali, M.F., Hasan, M.G., Shuo, W., Formaldehyde-to-Nitrogen dioxide ratio (FNR) analysis for ozone sensitivity: a case study over Bangladesh using OMI data, Air. Qual. Atmos. Hlth., 18, 1879-1886, https://doi.org/10.1007/s11869-025-01732-5, 2025.

https://doi.org/10.5194/egusphere-2025-5837
Preprint. Discussion started: 14 January 2026
© Author(s) 2026. CC BY 4.0 License.

Raza, A., Dahlquist, M., Lind, T., Ljungman, P.L.S.: Susceptibility to short-term ozone exposure and cardiovascular and respiratory mortality by previous hospitalizations, Environ. Health, 17, 37, https://doi.org/10.1186/s12940-018-0384-z, 2018.

Sillman, S.: The use of NO_y, H_2O_2, and HNO_3 as indicators for ozone-NO_x- hydrocarbon sensitivity in urban locations, J. Geophys. Res., 100 (D7), 14175-14188, https://doi.org/10.1029/94JD02953, 1995.

Skamarock, W.C., Klemp, J.B., Dudhia, J., Gill, D.O., Barker, D.M., Duda, M.G., Huang, X.-Y., Wang, W., Powers, J.G.: A Description of the Advanced Research WRF Version 3, National Center for Atmospheric Research, Boulder, CO, USA, 2008.

Solazzo, E., Crippa, M., Guizzardi, D., Muntean, M., Choulga, M., Janssens-Maenhout, G., Uncertainties in the Emissions Database for Global Atmospheric Research (EDGAR) emission inventory of greenhouse gases, Atmos. Chem. Phys., 21, 5655-5683, https://doi.org/10.5194/acp-21-5655-2021, 2021.

Souri, A.H., Choi, Y., Jeon, W., Li, X., Pan, S., Diao, L., Westenbarger, D.A.: Constraining NO_x emissions using satellite NO_2 measurements during 2013 DISCOVER-AQ Texas campaign, Atmos. Environ., 131, 371–381, https://doi.org/10.1016/j.atmosenv.2016.02.020, 2016.

Turner, M.C., Jerrett, M., Pope, C.A., Krewski, D., Gapstur, S.M., Diver, W.R., Beckerman, B.S., Marshall, J.D., Su, J., Crouse, D.L., Burnett, R.T.: Long-term ozone exposure and mortality in a large prospective study, Am. J. Respir. Crit. Care Med., 193, 1134–1142, https://doi.org/10.1164/rccm.201508-1633OC, 2016.

van Geffen, J., Eskes, H., Compernolle, S., Pinardi, G., Verhoelst, T., Lambert, J.-C., Sneep, M., ter Linden, M., Ludewig, A., Boersma, K.F., Veefkind, J.P.: Sentinel5P TROPOMI NO_2 retrieval: impact of version v2.2 improvements and comparisons with OMI and ground-based data, Atmos. Meas. Tech., 15, 2037–2060, https://doi. org/10.5194/amt-15-2037-2022, 2022.

Veefkind, J., Aben, I., McMullan, K., Förster, H., De Vries, J., Otter, G., Claas, J., Eskes, H., De Haan, J., Kleipool, Q., van Weele, M., Hasekamp, O., Hoogeveen, R., Landgraf, J., Snel, R., Tol, P., Ingmann, P., Voors, R., Levelt, P.F.: TROPOMI on the ESA Sentinel-5 precursor: a GMES mission for global observations of the atmospheric composition for climate, air quality and ozone layer applications, Remote Sens. Environ., 120, 70–83, https://doi.org/https://doi.org/10.1016/j.rse.2011.09.027, 2012.

Voshtani, S., Ménard, R., Walker, T.W., Hakami, A.: Use of Assimilation Analysis in 4D-Var Source Inversion: Observing System Simulation Experiments (OSSEs) with GOSAT Methane and Hemispheric CMAQ, Atmosphere, 14, 758, https://doi.org/10.3390/atmos14040758, 2023.

Wang, Y., Wang, J., Xu, X., Henze, D.K., Qu, Z., Yang, K.: Inverse modeling of SO_2 and NO_x emissions over China using multisensor satellite data - Part 1: Formulation and sensitivity analysis, Atmos. Chem. Phys., 20, 6631–6650, https://doi.org/10.5194/acp-20-6631-2020, 2020.

Wang, Y., Yu, C., Tao, J., Wang, Z., Si, Y., Cheng, L., Wang, H., Zhu, S., Chen, L.: Spatio-temporal characteristics of tropospheric ozone and its precursors in Guangxi, South China, Atmosphere, 9, 355, https://doi.org/10.3390/atmos9090355, 2018.

https://doi.org/10.5194/egusphere-2025-5837
Preprint. Discussion started: 14 January 2026
© Author(s) 2026. CC BY 4.0 License.

Wang, Z., Zhang, H., Shi, C., Ji, X., Zhu, Y., Xia, C., Sun, X., Zhang, M., Lin, X., Yan, S., Zhou, Y., Xing, C., Chen, Y., Liu, C.: Vertical and spatial differences in ozone formation sensitivities under different ozone pollution levels in eastern Chinese cities, Npj Clim. Atmos. Sci., 8, 30, https://doi.org/10.1038/s41612-024-00855-3, 2025.

Wu, H., Kong, L., Tang, X., Zhu, L., Zhu, J., Wang, Z.: Air quality forecasting with inversely updated emissions for China, Environ. Sci. Technol. Lett., 10 (8), 655–661, https://doi.org/10.1021/acs.estlett.3c00266, 2023.

Yu, X., Millet, D.B., Henze, D.K.: How well can inverse analyses of high-resolution satellite data resolve heterogeneous methane fluxes? Observing system simulation experiments with the GEOS-Chem adjoint model (v35), Geosci. Model Dev., 14, 7775–7793, https://doi.org/10.5194/gmd-14-7775-2021, 2021.

Zhao, S., Russell, M. G., Hakami, A., Capps, S. L., Turner, M. D., Henze, D. K., Percell, P. B., Resler, J., Shen, H., Russell, A. G., Nenes, A., Pappin, A. J., Napelenok, S. L., Bash, J. O., Fahey, K. M., Carmichael, G. R., Stanier, C. O., Chai, T.: A multiphase CMAQ version 5.0 adjoint, Geosci. Model Dev., 13, 2925–2944, https://doi.org/10.5194/gmd-13-2925-2020, 2020, 2020.

Zhao, Y., Nielsen, C.P., Lei, Y., McElroy, M.B., Hao, J.: Quantifying the uncertainties of a bottom-up emission inventory of anthropogenic atmospheric pollutants in China, Atmos. Chem. Phys., 11, 2295–2308, https://doi.org/10.5194/acp-11-2295-2011, 2011.